ChemComm

HIGHLIGHT

View Article Online
View Journal | View Issue

Cite this: *Chem. Commun.*, 2023, **59**, 2341

Recent advances in label-free imaging of cell–matrix adhesions

Ping Zhou, Lurong Ding, Yajuan Yan, Yafeng Wang and Bin Su *

Cell–matrix adhesions play an essential role in mediating and regulating many biological processes. The adhesion receptors, typically transmembrane integrins, provide dynamic correlations between intracellular environments and extracellular matrixes (ECMs) by bi-directional signaling. In-depth investigations of cell–matrix adhesion and integrin-mediated cell adhesive force are of great significance in biology and medicine. The emergence of advanced imaging techniques and principles has facilitated the understanding of the molecular composition and structure dynamics of cell–matrix adhesions, especially the label-free imaging methods that can be used to study living cell dynamics without immunofluorescence staining. This highlight article aims to give an overview of recent developments in imaging cell–matrix adhesions in a label-free manner. Electrochemiluminescence microscopy (ECLM) and surface plasmon resonance microscopy (SPRM) are briefly introduced and their applications in imaging analysis of cell–matrix adhesions are summarized. Then we highlight the advances in mapping cell–matrix adhesion force based on molecular tension probes and fluorescence microscopy (collectively termed as MTFM). The biomaterials including polyethylene glycol (PEG), peptides and DNA for constructing tension probes in MTFM are summarized. Finally, the outlook and perspectives on the further developments of cell–matrix adhesion imaging are presented.

Received 30th November 2022,
Accepted 27th January 2023

DOI: 10.1039/d2cc06499e

rsc.li/chemcomm

1. Introduction

The extracellular matrix (ECM) is a highly dynamic structure that exists in all tissues, and is composed of a three-dimensional scaffold of matrix molecules, including primarily collagen, fibronectin and glycosaminoglycans.[1] In addition to providing structural support for tissue integrity, the ECM continuously undergoes remodeling to maintain tissue homeostasis.[2] Dysregulation of the ECM structure, composition, stiffness and function results in some disease conditions, such as fibrosis and invasive cancer.[3,4] As shown in Fig. 1a, cells interact with the ECM *via* transmembrane receptors, typically integrin, thus forming physical connections to the cytoskeletal actin through a host of linker proteins and achieving information transmission *via* the signalling molecules and pathways.[2] In this model, the binding of cells to the ECM introduces discrete structures at the cell surface, namely cell–matrix

Key Laboratory of Excited-State Materials of Zhejiang Province, Institute of Analytical Chemistry, Department of Chemistry, Zhejiang University, Hangzhou 310058, China. E-mail: subin@zju.edu.cn

Ping Zhou

Ping Zhou received her BSc degree in Chemistry from Qingdao University in 2017 and PhD degree in Analytical Chemistry from Zhejiang University in 2022. She is now a postdoctoral fellow at Zhejiang University. Her current research interests are focused on ECL analysis of cell adhesive force.

Lurong Ding

Lurong Ding received her BSc degree in Applied Chemistry from Zhejiang University of Technology in 2020. She is currently a PhD student in the Department of Chemistry at Zhejiang University. Her research is focused on ECL analysis of cell-microenvironment interactions.

adhesions, which mediate direct interactions between cells and the extracellular microenvironment.[5,6] These adhesive interactions are essential for the generation of adhesion-mediated signals that regulate a variety of biological processes, such as cell migration,[7,8] tissue organization,[9] wound healing,[10,11] and tumorigenesis.[12] Thus, elucidating the structure and function of cell–matrix adhesions is of great significance in the fields of biology and medicine.

Cell–matrix adhesions are formed at the specialized and elongated regions along the ventral cell membrane, which are tethered tightly to the substrate surface with a gap of only 10–15 nm.[6] It has been recognized that these sites can be classified into different types in terms of their protein composition, size, life span and proteolytic properties (as shown in Fig. 1b).[13] The shortest-lived adhesion structures termed as focal contacts (FCs) are typically located behind the leading edge of spreading or migrating cells, whose assembly and disassembly occur within the timescale of seconds or minutes. The cellular traction forces are propagated through the focal adhesion (FA) structures, which are composed of multiple proteins to guarantee the stability. Fibrillar adhesions (FBs), a kind of larger and more stable adhesion structure that run in parallel to fibronectin bundles *in vivo*, are rich in tensin and $\alpha_5\beta_1$ integrin[14] and also the sites of localized matrix deposition and fibronectin fibrillogenes. Podosomes commonly found in macrophages consist of a dense F-actin core and actin-binding proteins within a ring of integrins. The composition of invadopodia is similar to that of podosomes, while the former occurs only in malignant cells. The formation of adhesion structures is known to be associated with the activation of the integrin family of ECM receptors. Distinct integrin subtypes are generated by selective pairing between α and β subunits, the extracellular domains of which can bind to various ECM ligands with different affinities.[15] Therefore, integrins provide a bi-directional conduit that transmits mechanochemical information across the cell membrane. During the mechanotransduction process, cells sense and respond to mechanical cues of the surrounding environment through integrin-based adhesion sites and finally adapt to the extracellular milieu. This process is crucial for a broad range of physiological events including cell migration,[16] proliferation and differentiation,[17] biofilm formation,[18] embryonic development,[19] immune response[20] and so on. In particular, the cell–matrix adhesion force as a vital physical signal indeed functions in regulating cell behaviors and maintaining tissue integrity. Therefore, in-depth investigation of cell–matrix adhesions requires not only the visualization of adhesion structures and compositions but also the mapping and further quantification of cell–matrix adhesion forces, promoting synergistically the study of cell mechanobiology.

Over the past few decades, many research efforts have been made for imaging cell–matrix adhesions based on the advanced microscopy techniques and principles.[13,21] A considerable part of these research studies requires immunofluorescent labelling of specific proteins in adhesion structures, which remains challenging for the dynamic analysis of living cells in the long-term. To address this limitation, the mapping of cell–matrix adhesions in a label-free manner has been conducted.[22,23] This review will focus on the recent advances in label-free imaging of cell–matrix adhesions, including electrochemiluminescence microscopy (ECLM) and surface plasmon resonance microscopy (SPRM). Considering the significance of

Yajuan Yan

Yajuan Yan received her BSc degree from the School of Chemistry and Chemical Engineering, Lanzhou University in 2021. She is currently a PhD student at Zhejiang University. Her research interests include ECL microscopy and cell analysis.

Yafeng Wang

Yafeng Wang received his BSc degree in Applied Chemistry from Zhejiang University of Technology in 2014 and PhD degree in Analytical Chemistry from Zhejiang University in 2020. He is now a postdoctoral fellow at Zhejiang University and his research interests are focused on unraveling ECL mechanisms and developing ultrasensitive ECL biosensors.

Bin Su

Bin Su received his BS, MS and PhD degrees from Jilin University, Changchun Institute of Applied Chemistry (Chinese Academy of Sciences) and Ecole Polytechnique Federale de Lausanne (EPFL), respectively. After three years of postdoctoral research at EPFL, he joined Zhejiang University in 2009 and was promoted to a full professor with tenure in 2012. His current research interests cover interfacial electrochemistry, electrochemiluminescence, biosensors and in vivo bioanalysis.

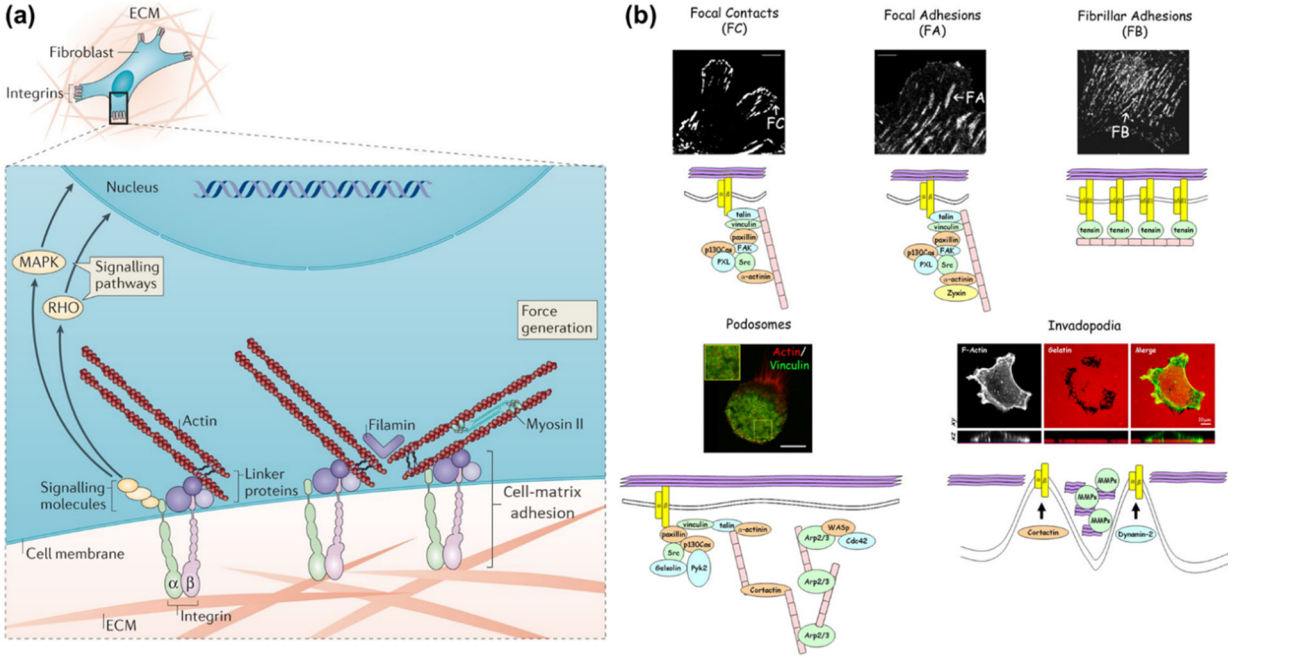

Fig. 1 (a) Schematic illustration of the cell-ECM interactions and associated intracellular structures. Adapted with permission from ref. 2 (Copyright 2014 Nature publishing group). (b) Confocal fluorescence images of different adhesion structures and their component cartoons. FC, FA and FB are shown by fibroblasts stained with β_3 integrin, β_1 integrin or tensin, respectively. THP-1 cells and A375M cells are stained with actin/vinculin and phalloidin to define podosomes and invadopodia, respectively. Reprinted with permission from ref. 13 (Copyright 2010 Company of Biologists Ltd).

revealing when and where cell adhesive force is generated at cell–matrix interfaces, in this article we will also highlight molecular tension fluorescence microscopy (MTFM) used for mapping the cell–matrix adhesion force. Finally, we shall present an outlook and perspective on the further development of cell–matrix adhesion imaging.

2. ECL microscopy

ECL is the light emission triggered by electrochemical reactions, which possesses unique advantages of excellent spatiotemporal controllability, low background and high surface sensitivity.[24–26] ECLM has recently manifested itself as a powerful tool in single cell analysis, including the identification of cellular contents and structures.[22,27–29] In previous works, small molecules in cells or released from cells,[30–32] (sub-)cellular structures including cell membranes,[33,34] proteins,[35–37] mitochondria[38] and intracellular hierarchical structures such as the nucleolus, nucleus and endoplasmic reticulum[39] have been visualized by ECLM.

When cells adhere to the underlying electrode surface, the formed adhesions can function as the inhibitors for ECL reactions and thus appear as dark shadows in ECL images. This mode is often designated as negative imaging.[40] Benefiting from the surface-confined nature of ECL-emitting regions dominated by the direct oxidative-reduction routes,[41] ECLM allows imaging of cell–matrix adhesion in the vicinity of the substrate surface (Fig. 2a).[42] The enhancement effects of silica nanochannel membranes (SNMs) on ECL intensity further favour a distinct visual contrast between cell adhesions and bare surfaces. With this methodology, the dynamic variation of cell–matrix adhesions during collective migration was explored. As reported recently, ECL emitting layers can be rationally modulated by changing the concentration ratio of ECL luminophore to coreactant to match with the spatial location of different cell junctions, so that cell–matrix adhesions and cell–cell junctions can be selectively imaged.[43] Ino *et al.* have studied the difference of cell adhesions between monolayer and tube network culture for vascular endothelial cells by ECLM, providing an identification method of adhesion states during tube formation.[44]

Further modifying the SNM rich in silanol groups with Arg-Gly-Asp (RGD), (3-aminopropyl)triethoxysilane (APTES), and oligo(ethylene glycol) (OEG), the influence of chemical microenvironments on cell behaviors was evaluated by imaging the cell–matrix adhesions.[46] The statistical analysis of spatial distribution, area and strength of adhesions shows that the surfaces tethered with RGD and OEG groups can mediate the robust and weakest cell-microenvironment interactions, respectively, and that an intermediate adhesion is distributed on the APTES-coated surface. Moreover, in conjunction with selective immune-blocking of different integrin subunits, α_6, α_5, and α_1 subunits are found to function in recognizing SNM, RGD/OEG and APTES surfaces, respectively.

Xia *et al.* have recently proposed an approach for positive imaging of cell adhesions by combined use of a closed bipolar nanoelectrode array and ECLM.[45] The bipolar electrode was fabricated by electrodeposition of gold into the channels of an anodic aluminum oxide (AAO) membrane and subsequently platinizing one of the two terminals. As depicted in Fig. 2b, the

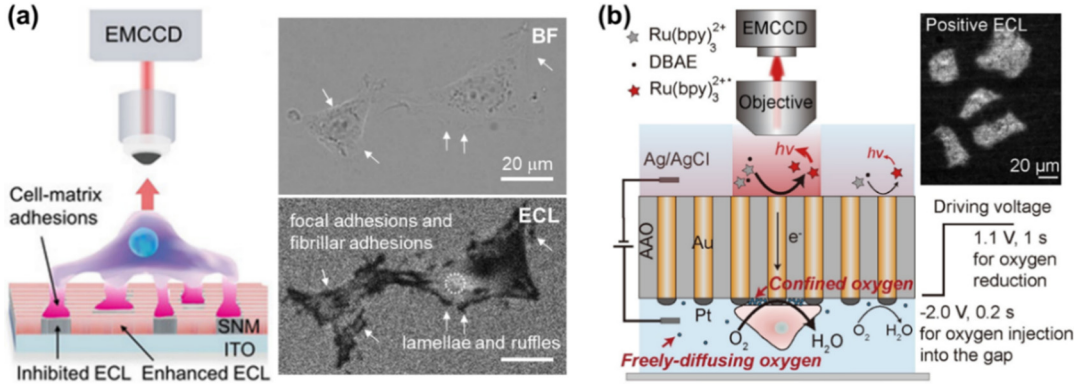

Fig. 2 (a) Schematic illustration of imaging cell–matrix adhesions by ECLM in the negative mode (left). The bright field (BF) and corresponding ECL image of cells (right). Reproduced from ref. 42 with permission from Wiley-VCH. (b) Scheme of ECL imaging of cell–matrix adhesions in the positive mode by using a closed bipolar nanoelectrode array. Reprinted from ref. 45 with permission from Wiley-VCH.

reduction of oxygen beneath cells occurs at the cathodic side, which is coupled with ECL reactions at the anodic one. A high concentration of oxygen in the confined space underneath cells contributes to the enhanced ECL intensity, thus realizing the imaging of cell adhesions in a positive contrast mode. Cell morphology and adhesion strength can be also successfully imaged with this method.

3. SPR microscopy

SPRM has drawn considerable research interest since it was firstly described by Rothenhäusler *et al.*[47] Under SPR, the surface plasmon wave travels along the metal-dielectric layer interface and decays exponentially.[48] The evanescent wave is extremely sensitive to the tiny variation of physical parameters of the metal-dielectric multilayers, thus making SPR a non-invasive technique for biosensing near the metal surface.[23] It has been widely used so far to study subcellular structures[49–51] and dynamic cellular processes.[52–56]

Giebel *et al.* analysed quantitatively the cell-substrate distance by SPRM, which was found to be 160 ± 10 nm for most parts of the cell, except for the peripheral lamellipodia (only 25 ± 10 nm).[58] Subsequently renovated SPRMs, lens-imaging-type SPRM (Fig. 3a, left) and scanning localized SPRM (Fig. 3a, right), were used to measure the cell-electrode cleft gap distance.[57] The former allows simultaneous large-area observation of the cellular bottom membrane, by which the strength of cell adhesions has been assessed qualitatively in terms of the reflected light intensity contrast (Fig. 3b). The latter is capable of mapping the cleft gap distance quantitatively with a high spatial resolution by selecting a region of interest (Fig. 3c), which can be used to study the difference of cell adhesions on gold surfaces coated with various peptides or proteins. It has been reported that the combination of them can contribute to observing an entire cell adhesion site and identifying regions of interest.[59] The measurement accuracy of SPRM was later increased by decoupling the cell–substrate distance and the refractive index of the cytoplasm, by which the three-dimensional profiles of the basal membrane

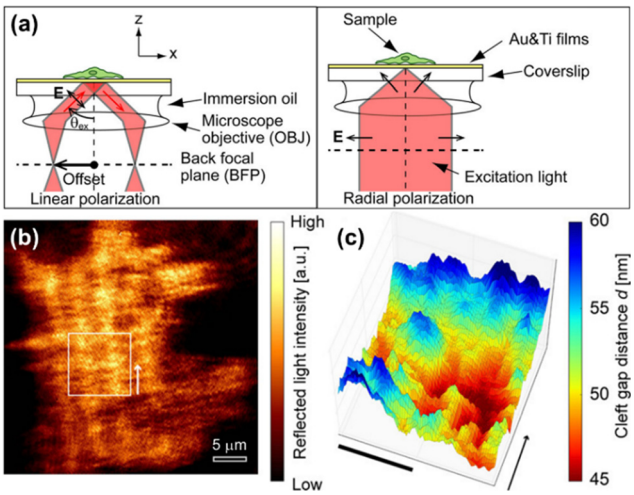

Fig. 3 (a) Schematic illustration of optical paths nearby the sample for lens-imaging-type (LISPM, left) and scanning localized (SLSPM, right) SPRM. (b and c) Representative LISPM (b) and SLSPM (c) images of HEK293 cells cultured on a poly-L-lysine-coated gold surface. Adapted with permission from ref. 57 (Copyright 2014 American Chemical Society).

and its dynamics were reconstructed with an actual measurement accuracy of 2.3 nm.[60] SPRM also allows simultaneous mapping of the cell-substrate adhesion gap, projected area, gap surface area and gap volume, thus providing a comprehensive analysis of the cell adhesion behaviors.[61] In addition, the local movement of the cell membrane caused by extracellular osmotic pressure can be monitored with SPRM, so that the displacement image is considered to be the distribution of the cell adhesion strength.[62] Recently, the impact of chemical fixation required for electron microscopy on the cell–substrate interface was investigated with SPRM, showing a retentive structure after chemical fixation.[63]

Using SPRM, the changes of cell–matrix adhesions mediated by cell–cell communication and the adhesion dynamics induced by shear stress were studied in real-time.[64] A positive correlation between the FA mass and protein density was unveiled, showing a distinct difference for different cell types.[65] Wavelength-scanning SPRM has also been developed for measuring the

cell-substrate interaction, with a dynamic range larger than intensity-based SPRM.[66] Plasmonic scattering microscopy (PSM), with a sub-micrometer spatial resolution and a microsecond temporal resolution, makes it possible to study cellular deformations induced by osmotic pressure changes or immune activation, as well as focal adhesion binding strength and rate, at the individual focal adhesion level.[67,68] In addition, mapping the cell adhesion spring constants with PSM can provide an approach for the quantitative analysis of cell adhesion mechanical properties.[68]

4. MTFM for mapping the cell–matrix adhesion force

To date, substantial research interests have been drawn to study cell adhesive force and related physiological functions. To visualize the miniscule level of force ranging from pN to nN, different methods have been developed, such as traction force microscopy (TFM)[69–71] and single molecule force spectroscopy (SMFS) including atomic force microscopy,[72–74] optical or magnetic tweezers,[75,76] *etc.* Among them, TFM is only sensitive to forces at the nN level, while the SMFS methods fail to capture the mechanics of a whole cell because of their low throughput.

MTFM works relying on molecular tension probes labeled with a fluorophore, fluorophore–fluorophore or fluorophore–quencher pair.[77,78] Cell adhesive force transmits through the specific interactions between ligands in MTFM probes and receptors on cell membranes. For instance, the RGD peptide motif can recognize multiple integrin subtypes.[79] Using MTFM, the cell–matrix adhesive force can be visualized with a sub-micrometer spatial resolution, pN force sensitivity and high throughput.[80,81] Polyethylene glycol (PEG), peptide and DNA structures have been extensively used for constructing the molecular tension probes in MTFM. Corresponding information about force response and signal acquisition of molecular tension probes is summarized in Table 1.

4.1 PEG-based MTFM

Thanks to the unique properties, such as well-characterized and reversible mechanical performance, biocompatibility and stability, PEG has been extensively used in MTFM. For example, PEG-based MTFM was engineered to map the cell adhesive force during the initial stages of regulatory endocytosis of the epidermal growth factor receptor (EGFR) for the first time.[82] As shown in Fig. 4a, the PEG polymer is flanked with a fluorescently labeled EGF ligand and a biotin moiety for surface immobilization. When a cell exerted the force on the ligand, the PEG linker in the relaxed conformational state can be extended, thus resulting in the removal of the fluorophore from proximity to the quencher and the increase of fluorescence (FL) intensity (Fig. 4a). Punctate force signals were observed upon EGFR engagement (Fig. 4b), which was confirmed to be associated with the clathrin-mediated EGF ligand internalization. Based on the high affinity of the RGD peptide ligand to $\alpha_V\beta_3$ and $\alpha_5\beta_1$ integrins, MTFM was used to study the integrin-generated force in cell adhesions, which was found to be sufficient to dissociate streptavidin–biotin tethered ligands.[85] Using gold nanoparticles as a quencher, the dynamics of tensions exerted by integrin receptors during cell adhesion can be imaged, showing a translocation from the center of the cell to its periphery.[86] In addition, the immobilization of tension probes on gold nanoparticles (AuNPs) through gold–thiol binding can minimize the possibility of probe rupture. Then, combining the above MTFM with block copolymer micelle nanolithography, a substrate with arrays of precisely spaced probes was fabricated to study the impact of integrin clustering on force transmission.[87] Critical ligand spacing (<60–70 nm) helps in sustaining high integrin forces,

Table 1 Molecular tension probes used in MTFM

Tension probe	Force range or threshold/pN	Fluorophore or FRET donor	Quencher or FRET acceptor	Ref.
PEG	0–20	Alexa 647	QSY 21	82
	~1–30	Alexa 647	QSY 21	85
	~25	Alexa 488	AuNP	86
	~27	Cy3B	AuNP	87
Peptide	1–7	Alexa 546	Alexa 647	83
	1–5	Alexa 546	CoA 647	89
	2–7/7–11	Alexa 546	Alexa 647	90
	~80–200	Alexa 488/647; Cy3	AuNP	84
dsDNA	12–54	Cy3/Cy5	—	97 and 98
	43, 54, >100	Cy3/Cy5	—	99
	54	Cy5	BHQ2	
	12, 54	Cy3	BHQ2	100 and 106
	54, 100	Cy3	BHQ2	101
	12, 54	Cy3, Atto647N	BHQ2	102
	12, 54, 160	Cy3B	BHQ2	103
PNA/DNA	12	Alexa 488	BHQ2	105
	12	Cy5	BHQ2	104
DNA hairpin	4.7 ± 1.7, 13.1 ± 2.4	Cy3B/Cy5	BHQ1/QSY21	107
	4.7, 13.1, 19.3	Cy3B	BHQ2	109
	12, 19, 56	Cy3B	BHQ2, AuNP	110
	4.7	Cy3B, Atto647N	BHQ2	111
RSDTP	4–60	Cy3B, Atto647N	BHQ2	115

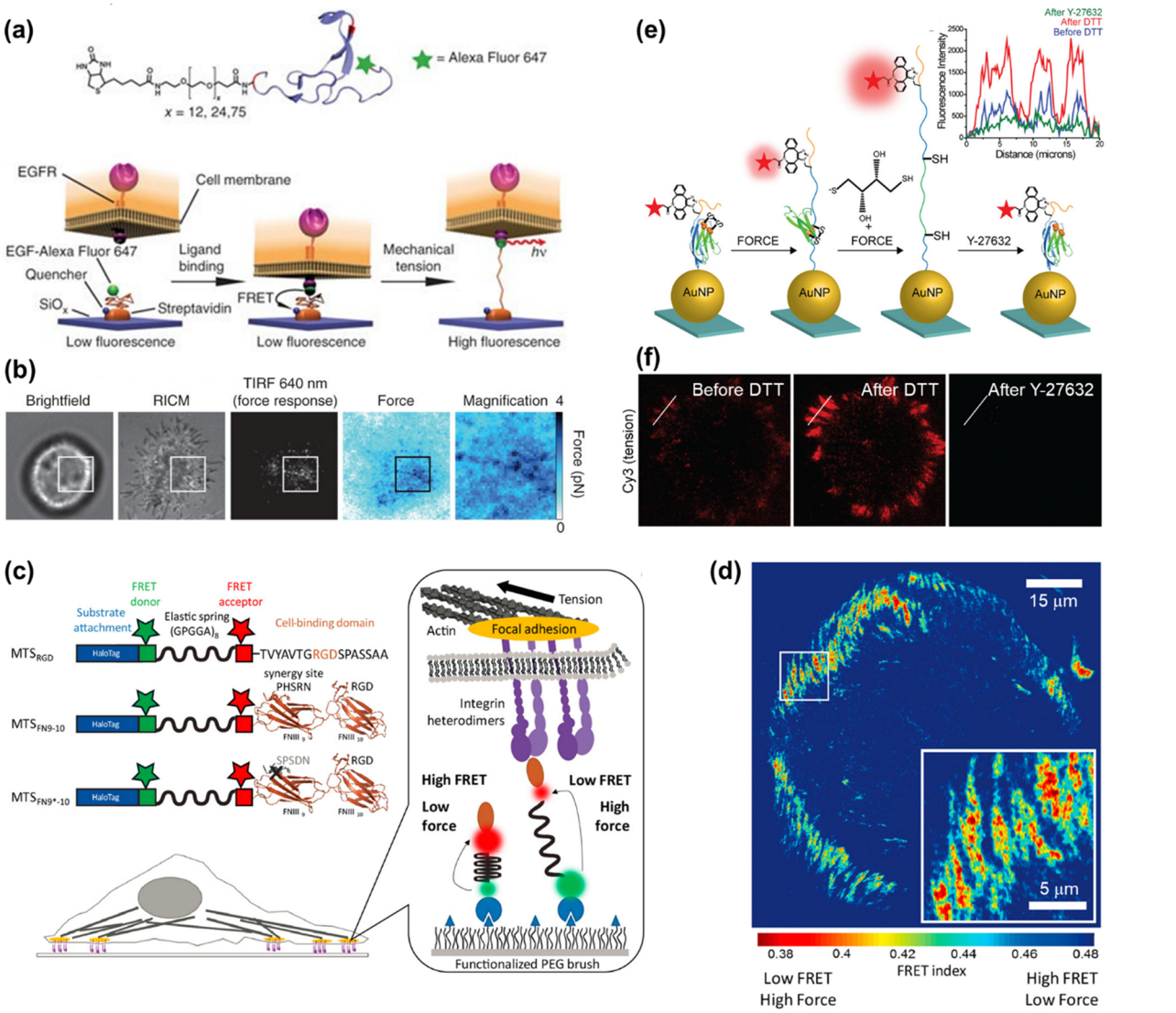

Fig. 4 (a) The mechanism of PEG-based MTFM with the PEG polymer flanked by a fluorescently labeled (Alexa Fluor 647) EGF ligand and a biotin moiety for surface immobilization *via* streptavidin capture. (b) Representative brightfield, reflection interference contrast microscopy (RICM), FL response and force map converted from the FL image for a cell engaged to a sensor surface modified with the PEG-based tension probes. (a and b) Adapted with permission from ref. 82 (Copyright 2012 Nature publishing group). (c) Schematic composition of tension probes in peptide-based MTFM for studying the force generated by individual integrins. (d) Traction force map represented by FRET index obtained for cell spread on the surface modified with peptide-based tension probes. (c and d) Adapted with permission from ref. 83 (Copyright 2016 American Chemical Society). (e) The mechanism of the disulfide clamped I27 tension sensor in the presence of dithiothreitol (DTT) or Y-27632. (f) Representative I27-based tension signal for REF cells incubated on the sensor surface for 2 h before and after treating with 0.25 mM DTT for 10 min and subsequently with Y-27632 (40 μM) for 30 min. FL intensity profiles along the white lines are displayed in the inset of (e). (e and f) Reproduced from ref. 84 with permission from American Chemical Society.

thus facilitating the maturation of focal adhesion, while integrin receptors placed >100 nm apart significantly reduce the tension and destabilize the focal adhesion formation. This work realizes the simultaneous measurement of pN adhesive forces while regulating receptor nanoclustering.

4.2 Peptide-based MTFM

Peptide molecules can also function as entropic springs for measuring the adhesive force. Grashoff *et al.* designed a tension-sensitive probe composed of repetitive amino-acid motifs, $(GPGGA)_8$ peptide, which was derived from the spider silk protein flagelliform for force sensing.[88] The elastic domain linked with two fluorescent proteins as a fluorescence resonance energy transfer (FRET) pair was genetically inserted into vinculin. This work revealed that stable focal adhesions required a force of ~2.5 pN transmitted across vinculin. Using the same peptide sequence flanked with two organic dyes as the FRET pair, Dunn's group developed a molecular tension sensor to investigate the force generated by individual integrins (as seen in Fig. 4c).[83,89,90] Defining the ratio of acceptor intensity to the sum of donor and acceptor intensity as FRET index, a traction force map can be drawn (Fig. 4d), which reflects the distribution of tension. In terms of the FRET values, the authors proposed that relatively modest tensions at the molecular level were sufficient to drive

robust cell adhesions.[83,89] Further analysis indicated that the addition of synergy sites to $\alpha_5\beta_1$ integrin resulted in increased integrin recruitment to adhesions, instead of enhancing overall cellular traction generation.[83] The experienced loads of integrins below their peak capacities guarantee the mechanical integrity of cells and tissues, which was uncovered by a revised model.[90] Limited by the minimal dynamic range of the above-mentioned peptide-based tension probe ($\sim$1–5 pN), the magnitude of integrin forces within cell adhesions remains unclear. A mechanically stable molecular tension probe consisting of the immunoglobulin 27th (I27) domain of cardiac titin flanked with a fluorophore and gold nanoparticle was reported (Fig. 4e).[84] A threshold force of up to $>$100 pN is required to unfold I27.[91] The integrin-mediated forces were confirmed to be more than 30–40 pN. Subsequently, a covalent disulfide bridge that can resist pN mechanical unfolding was added to I27 to ''clamp'' the probe (as shown in Fig. 4e). Incubation with a reducing agent (such as dithiothreitol) triggers the thiol exchange and the opening of the clamp, thus leading to full de-quenching of the fluorophore. Following Rho-associated protein kinase (ROCK) inhibition with Y-27632, the FL signal can diminish again, confirming that the opening of the clamped probes is driven by myosin and the signal is reversible (Fig. 4f). The rate of S–S reduction allows estimation of the applied integrin force in focal adhesions, which is *ca.* 110 $\pm$ 9 pN. This work provides a general approach for studying the high-level integrin tensions existing in stable cell adhesions.

4.3 DNA-based MTFM

DNA-based MTFM has emerged as a powerful tool for sensing the cell adhesive force because of its simple and versatile design, and tunable and programmable mechanical features.[78,92] The tension tolerance (T_{tol}) of DNA can be regulated by adjusting the DNA sequence or the force application site on the DNA backbone.[93–95] The probes will rupture once the cell tension exceeds T_{tol}. Double-stranded DNA (dsDNA) was used for the measurement of adhesive force for the first time by Ha *et al.* and they termed it as a tension gauge tether (TGT).[96] Subsequently, a range of TGTs with tunable tolerances have been engineered, by which the force transmitted by a single integrin–ligand during initial adhesion (a universal peak of about 40 pN) and the required force for Notch activations (less than 12 pN) can be determined.[96,97] A mixture of TGTs with T_{tol} values of 12 pN and 54 pN labeled with Cy5 and Cy3 fluorophores, respectively, and coated on the substrate surface can be used to simultaneously map the integrin tensions, proving that integrins both inside and outside focal adhesions contribute to tensions in stable cell adhesion.[98] RGD peptide is a ligand that has affinity to $\alpha_V\beta_3$ and $\alpha_5\beta_1$ integrins, so the specific identification of the integrin subtype remains elusive. Recently, Kim *et al.* developed a novel TGT probe based on an ATN-16 ligand for specific binding to $\alpha_5\beta_1$ integrin.[99] As seen in Fig. 5a, a force tolerance of 43 pN or 54 pN can be controlled by the location of biotins on the bottom DNA strand, while T_{tol} of $>$100 pN was estimated by disassociation of the biotin–streptavidin bond. DNA rupture caused by integrin tension greater than T_{tol} resulted in the loss of the FL signal of the fluorophore (Cy3 or Cy5) conjugated to one terminal of the upper DNA strand, by which the distribution of integrin tension was imaged. As shown in Fig. 5b, $\alpha_V\beta_3$ integrin tension contributed to a ring-shaped ''edge rupture'' (RGD-TGT surface), whereas a ''ventral rupture'' was observed on the ATN-TGT surface. To evaluate the correlation between ventral rupture and invadopodia, an ATN-quenched TGT (ATN-qTGT) was developed on the basis of a fluorescent dye-quencher pair (Fig. 5c). In this configuration, the FL signal was observed when ATN-qTGT was dissociated by cellular force (Fig. 5d). Further analysis indicates that $\alpha_5\beta_1$ integrin tension above 40 pN is required for the formation and maturation of invadopodia. The qTGTs with various T_{tol} values were also applied to map cell adhesive force in the single platelet[100] and migrating keratocytes.[101] The spatial resolution was calibrated to be *ca.* 0.4 μm. The results provide direct evidence that high-level integrin tension ($>$54 pN) is concentrated at the cell rear margin to detach cell adhesion, thus facilitating the cell rear retraction during the migration process.[101] Ha *et al.* have revealed the force propagating mechanism during smooth muscle cell shortening induced by histamine through real-time imaging of FA dynamics.[102] They proposed that FA reinforcement caused the time delay in cell shortening. Cell traction forces are of great significance for the development of functional cardiac muscle cells (CMCs) and the specific magnitude of integrin tension at pN level remains ambiguous. qTGT-based MTFM was used to address this knowledge gap.[103] It has been shown that adhesion tethers with greater force tolerance (T_{tol} $>$ 56 pN) can lead to functionally mature CMCs.

To resist the degradation of DNA from DNase on the cell membrane, a peptide nucleic acid (PNA)/DNA hybrid-based tension probe was developed for constructing MTFM.[104,105] Wang *et al.* have reported that the formation of a podosome is independent of extracellular integrin–ligand tensions, although they are critical for the formation of FA.[105] Furthermore, PNA/DNA-based MTFM with a high spatial resolution of *ca.* 50 nm was developed by multiple cycles of molecular tension imaging and localization (as seen in Fig. 5e).[104] Ultranarrow distribution of integrin tensions at the cell leading edge was revealed for both migratory cells and stationary cells. The irreversibility of dsDNA rupture makes it unavailable to image cell adhesive force continuously, so that the real-time force mapping can be realized by recording the time-lapse images of tension signals and then acquiring the new force map with the frame subtraction method.[102,106]

DNA hairpin is a single-stranded DNA consisting of intramolecular base pairs, which has been employed as a ''switch'' element for imaging the cell adhesive force. As shown in Fig. 6a, the fluorophore–quencher pair is conjugated to the DNA hairpin structure, thus reporting the force distribution by the FL signal when the DNA hairpin is unfolded. The tension threshold can be tuned by altering the GC content in the DNA sequence (Fig. 6b).[107] Using DNA hairpin-based MTFM, highly dynamic and heterogeneous integrin tension has been visualized.[107,108] As shown in Fig. 6c, the force signal is located at the cell edges and its intensity increases rapidly within minutes. Further determination of the percentage of unfolded

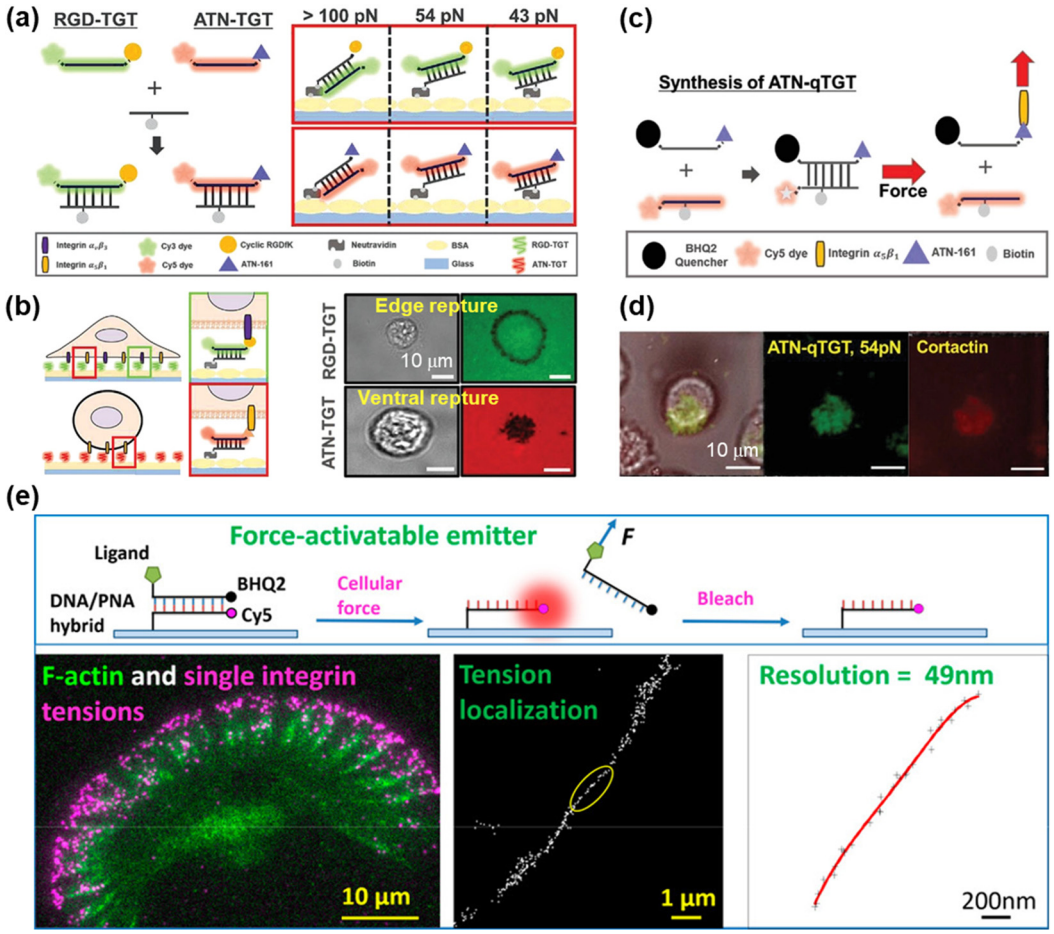

Fig. 5 (a) Schematic diagrams of the dsDNA-based TGT systems. (b) The working principle of dsDNA-based TGT for the measurement of integrin tensions (left) and corresponding tension signals (right) during cell adhesion. (c) Illustration of the synthesis and tension-induced rupture of ANT-qTGT. (d) Invadopodia marker (cortactin) and tension response (ATN-qTGT) were co-localized. (a–d) Adapted with permission from ref. 99 (Copyright 2022 Wiley-VCH). (e) The force-activated rupture of PNA/DNA hybrid-based tension probe (top). Single integrin tension mapping in a migrating keratocyte with a calibrated resolution of 49 nm (bottom). Reprinted with permission from ref. 104 (Copyright 2020 American Chemical Society).

probes by calculating the FL intensity of de-quenched dyes corresponding to a fully opened hairpin probe indicates that a large density of hairpins of up to 9% have been unzipped at these regions. A DNA hairpin-based tension probe was also used to map the force distribution during the process of platelet activation.[109] A tension greater than 19 pN was produced at the central zone of the platelet, while a weak force (~4.7–13.1 pN) was located at the cell periphery. In addition, Salaita *et al.* have uncovered the important role of cell adhesive force in T cell activation.[110,111] In recent years, super-resolution visualization of single integrin tension has received considerable research attention.[112–114] In conjunction with DNA-PAINT super-resolution microscopy,[113] mechanical engagement of single integrin receptors has been studied.[114] It is found that in cell adhesions the integrin receptor clustering is governed by a non-random organization with complexes spaced as close as 20–30 nm.

In contrast to dsDNA, the opening of a DNA hairpin triggered by tensions is reversible, thus allowing the continuous imaging of the cell adhesive force. However, a broader tension range of dsDNA (10–60 pN) than the DNA hairpin (4–18 pN) makes it well suited for studying the dynamic behaviors of the cellular mechanotransduction process.[77,80,81] To address the shortcoming in real-time measurements of cell force with a value of higher than 20 pN, Liu *et al.* have developed a reversible shearing DNA tension probe (RSDTP).[115] Fig. 6d displays the force-response mechanism of RSDTP, the thresholds of which can be regulated by varying both the GC content and force application site of the probe. After seeding NIH-3T3 cells on a RSDTP-functionalized surface for 1 h, the tension signal was observed at the cell edge (Fig. 6e), in agreement with that reported previously.[86,107,108] Moreover, the tension pattern obtained with 56 pN RSDTPs indicates that mechanically strong integrin clusters (>56 pN) exist in FAs (Fig. 6e), which can serve as the "mechanical hotspots" to maintain the architecture of FAs and facilitate their maturation.

5. Conclusions and outlook

A range of techniques being developed currently and used successfully have opened an avenue for the studying of cell–

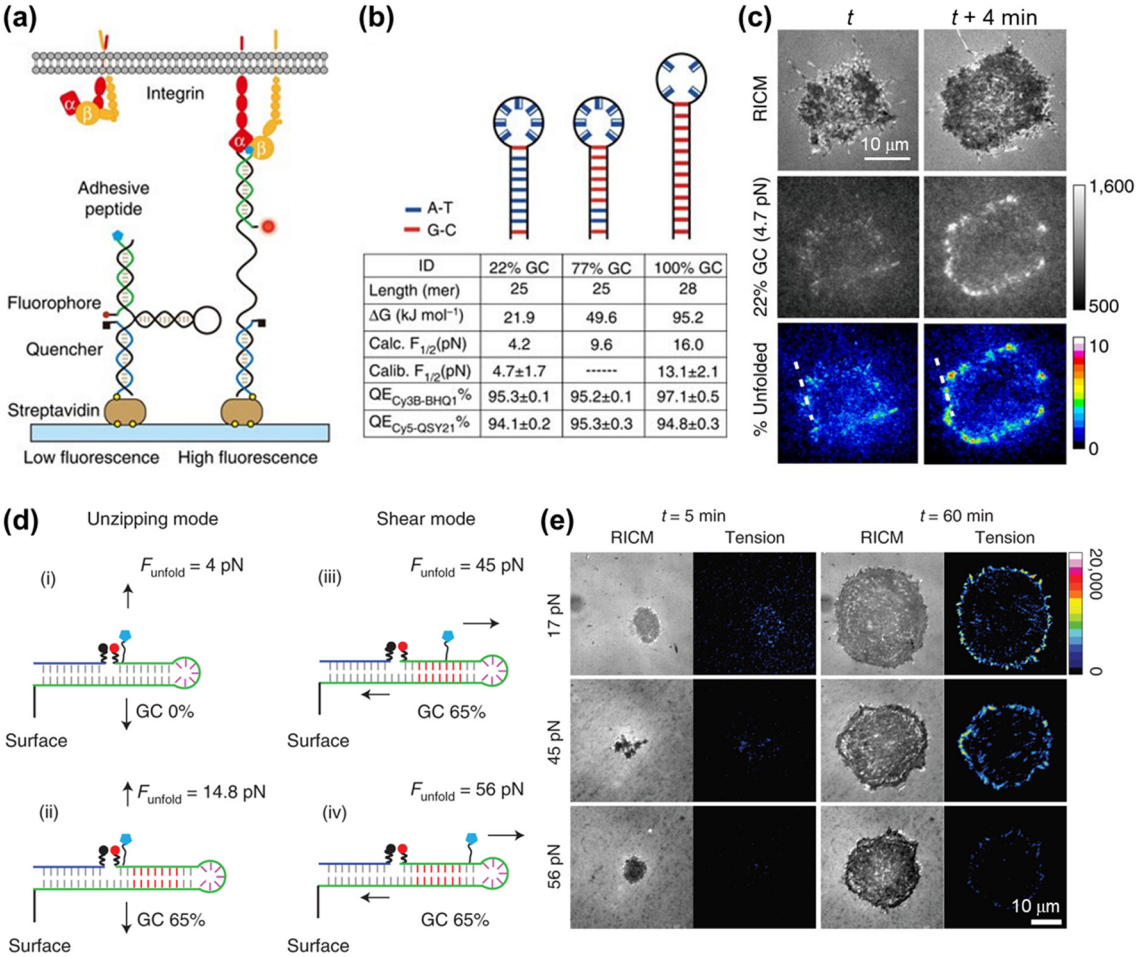

ID	22% GC	77% GC	100% GC
Length (mer)	25	25	28
ΔG (kJ mol^{-1})	21.9	49.6	95.2
Calc. $F_{1/2}$(pN)	4.2	9.6	16.0
Calib. $F_{1/2}$(pN)	4.7±1.7	------	13.1±2.1
$QE_{Cy3B\text{-}BHQ1}$%	95.3±0.1	95.2±0.1	97.1±0.5
$QE_{Cy5\text{-}QSY21}$%	94.1±0.2	95.3±0.3	94.8±0.3

Fig. 6 (a) Schematic illustration of the DNA hairpin-based tension sensor consisting of an anchor strand immobilized onto a surface (blue), a hairpin strand (black) and a ligand strand representing an adhesive peptide (green). The fluorophore and quencher are bonded to the opposing termini of the ligand and anchoring strands. (b) The table lists the tension thresholds and quenching efficiency with the variation of the GC content. (c) Representative RICM and MTFM (4.7 pN probe) time-lapse images at the indicated time points. The percentage of unfolded tension probes ("% unfolded" channel) indicates the fraction of 22% GC hairpins that have been unfolded within each pixel. (a–c) Reproduced with permission from ref. 107 (Copyright 2014 Nature publishing group). (d) The force-application geometries of RSDTPs with different tension tolerances. (e) Time-lapse images of RICM and tension map during the spreading of NIH-3T3 cells on substrates modified by RSDTPs with different unfolding forces. (d and e) Adapted with permission from ref. 115 (Copyright 2021 Nature publishing group).

matrix adhesions, in particular the visualization analysis of their structures and dynamics. In comparison with the mainstream fluorescence microscopy that requires immunofluorescent labeling of specific adhesive proteins, the label-free approaches are suitable for observing living cells. ECLM has manifested itself as a surface-sensitive tool for single cell analysis, by which the imaging of cell–matrix adhesions with the negative or positive mode has been realized. Dynamic variations of cell–matrix adhesions during some biological processes such as collective migration and tube formation can be mapped using ECLM. SPRM can provide a quantitative method for the measurement of cell-substrate distances with a high spatial and temporal resolution, with which the strength and dynamic evolution of cell adhesions are revealed. Combined and developed microscopy imaging methods based on SPRM can further improve the spatiotemporal resolution.

Integrin-mediated cell–matrix adhesions can serve as a bi-directional conduit between the intracellular environment and extracellular matrix during cellular mechanotransduction. MTFM has emerged as a powerful sensor for visualizing and quantifying the cell adhesive force with a sub-micrometer spatial resolution, pN force sensitivity and high throughput, thus uncovering the elusive molecular mechanisms. Among these biomaterials including PEG, peptide and DNA, DNA and DNA-like structures are particularly versatile to be employed as molecular tension probes thanks to their simple and versatile designs, and tunable and programmable force response thresholds, which have drawn considerable research interest in real-time measurement of cell–matrix adhesion force. However, the current investigations show that the visualization of net orientations of averaged adhesive forces and even individual molecular tensions by MTFM is yet to be resolved and still remains challenging.

Certainly, integrins are the major proteins mediating cell–matrix adhesion, which are clustered and form patterns in various cell adhesive units such as FCs, FAs, FBs, podosomes

and invadopodia. Imaging cell–matrix adhesions and mapping cell adhesive force at a single-integrin level rather than the integrin clusters will contribute to the investigation and understanding of the molecular mechanisms in adhesion dynamics. Nevertheless, the imaging methods mentioned in this article, ECLM, SPRM and MTFM, are all restricted by the optical diffraction limits, and are not suitable for imaging cell–matrix adhesions with super-high spatial resolution down to 200 nm, thus making super-resolution imaging challenging. Representative super-resolved imaging techniques such as stochastic optical reconstruction microscopy (STORM), stimulated emission depletion (STED) microscopy and photoactivated localization microscopy (PALM) have already been applied in imaging biological structures.[116] It seems naturally feasible to image cell–matrix adhesions at the single-molecule level with resolution beyond the diffraction limit by combining ECLM, SPRM and MTFM with super-resolution methodologies. In addition, cryo-electron microscopy has recently made great breakthroughs in studying the adhesion structures and the transmission of mechanical force within cell adhesion,[117–119] which will facilitate a profound insight into the adhesive mechanisms.

Conflicts of interest

There are no conflicts of interest to declare.

Acknowledgements

This work is supported by the National Natural Science Foundation of China (No. 22125405, 22074131 and 21874117).

References

1 C. Frantz, K. M. Stewart and V. M. Weaver, *J. Cell Sci.*, 2010, **123**, 4195–4200.
2 J. D. Humphrey, E. R. Dufresne and M. A. Schwartz, *Nat. Rev. Mol. Cell Biol.*, 2014, **15**, 802–812.
3 C. Bonnans, J. Chou and Z. Werb, *Nat. Rev. Mol. Cell Biol.*, 2014, **15**, 786–801.
4 J. Huang, L. Zhang, D. Wan, L. Zhou, S. Zheng, S. Lin and Y. Qiao, *Signal Transduction Targeted Ther.*, 2021, **6**, 153.
5 A. L. Berrier and K. M. Yamada, *J. Cell. Physiol.*, 2007, **213**, 565–573.
6 E. Zamir and B. Geiger, *J. Cell Sci.*, 2001, **114**, 3583–3590.
7 E. K. Paluch, I. M. Aspalter and M. Sixt, *Annu. Rev. Cell Dev. Biol.*, 2016, **32**, 469–490.
8 J. R. W. Conway and G. Jacquemet, *Essays Biochem.*, 2019, **63**, 535–551.
9 E. Papusheva and C.-P. Heisenberg, *EMBO J.*, 2010, **29**, 2753–2768.
10 T. Omelchenko, J. M. Vasiliev, I. M. Gelfand, H. H. Feder and E. M. Bonder, *Proc. Natl. Acad. Sci. U. S. A.*, 2003, **100**, 10788–10793.
11 M. Poujade, E. Grasland-Mongrain, A. Hertzog, J. Jouanneau, P. Chavrier, B. Ladoux, A. Buguin and P. Silberzan, *Proc. Natl. Acad. Sci. U. S. A.*, 2007, **104**, 15988–15993.
12 P. Friedl, J. Locker, E. Sahai and J. E. Segall, *Nat. Cell Biol.*, 2012, **14**, 777–783.
13 D. C. Worth and M. Parsons, *J. Cell Sci.*, 2010, **123**, 3629–3638.
14 J. A. Green and K. M. Yamada, *Adv. Drug Delivery Rev.*, 2007, **59**, 1293–1298.
15 B.-H. Luo, C. V. Carman and T. A. Springer, *Annu. Rev. Immunol.*, 2007, **25**, 619–647.
16 C. D. Pascalis and S. Etienne-Manneville, *Mol. Biol. Cell*, 2017, **28**, 1833–1846.
17 R. McBeath, D. M. Pirone, C. M. Nelson, K. Bhadriraju and C. S. Chen, *Dev. Cell*, 2004, **6**, 483–495.
18 M. Asally, M. Kittisopikul, P. Rué, Y. Du, Z. Hu, T. Çağatay, A. B. Robinson, H. Lu, J. Garcia-Ojalvo and G. M. Süel, *Proc. Natl. Acad. Sci. U. S. A.*, 2012, **109**, 18891–18896.
19 T. Mammoto and D. E. Ingber, *Development*, 2010, **137**, 1407–1420.
20 E. Judokusumo, E. Tabdanov, S. Kumari, M. L. Dustin and L. C. Kam, *Biophys. J.*, 2012, **102**, L5–L7.
21 O. Medalia and B. Geiger, *Curr. Opin. Cell Biol.*, 2010, **22**, 659–668.
22 H. Ding, B. Su and D. Jiang, *ChemistryOpen*, 2022, e202200113.
23 M. Bocková, J. Slabý, T. Špringer and J. Homola, *Annu. Rev. Anal. Chem.*, 2019, **12**, 151–176.
24 M. M. Richter, *Chem. Rev.*, 2004, **104**, 3003–3036.
25 M. Hesari and Z. Ding, *J. Electrochem. Soc.*, 2015, **163**, H3116–H3131.
26 W. Miao, *Chem. Rev.*, 2008, **108**, 2506–2553.
27 J. Zhang, S. Arbault, N. Sojic and D. Jiang, *Annu. Rev. Anal. Chem.*, 2019, **12**, 275–295.
28 H. Ding, W. Guo and B. Su, *ChemPlusChem*, 2020, **85**, 725–733.
29 C. Ma, Y. Cao, X. Gou and J.-J. Zhu, *Anal. Chem.*, 2020, **92**, 431–454.
30 R. He, H. Tang, D. Jiang and H.-Y. Chen, *Anal. Chem.*, 2016, **88**, 2006–2009.
31 J. Xu, P. Huang, Y. Qin, D. Jiang and H.-Y. Chen, *Anal. Chem.*, 2016, **88**, 4609–4612.
32 G. Liu, C. Ma, B.-K. Jin, Z. Chen and J.-J. Zhu, *Anal. Chem.*, 2018, **90**, 4801–4806.
33 S. Voci, B. Goudeau, G. Valenti, A. Lesch, M. Jović, S. Rapino, F. Paolucci, S. Arbault and N. Sojic, *J. Am. Chem. Soc.*, 2018, **140**, 14753–14760.
34 C. Ma, M.-X. Wang, H.-F. Wei, S. Wu, J.-R. Zhang, J.-J. Zhu and Z. Chen, *Chem. Commun.*, 2021, **57**, 2168–2171.
35 G. Valenti, S. Scarabino, B. Goudeau, A. Lesch, M. Jović, E. Villani, M. Sentic, S. Rapino, S. Arbault, F. Paolucci and N. Sojic, *J. Am. Chem. Soc.*, 2017, **139**, 16830–16837.
36 J. Zhang, R. Jin, D. Jiang and H.-Y. Chen, *J. Am. Chem. Soc.*, 2019, **141**, 10294–10299.
37 Y. Liu, H. Zhang, B. Li, J. Liu, D. Jiang, B. Liu and N. Sojic, *J. Am. Chem. Soc.*, 2021, **143**, 17910–17914.
38 Y. Ma, C. Colin, J. Descamps, S. Arbault and N. Sojic, *Angew. Chem., Int. Ed.*, 2021, **60**, 18742–18749.
39 C. Ma, S. Wu, Y. Zhou, H.-F. Wei, J. Zhang, Z. Chen, J.-J. Zhu, Y. Lin and W. Zhu, *Angew. Chem., Int. Ed.*, 2021, **60**, 4907–4914.
40 L. Xu, Y. Li, S. Wu, X. Liu and B. Su, *Angew. Chem., Int. Ed.*, 2012, **51**, 8068–8072.
41 W. Guo, P. Zhou, L. Sun, H. Ding and B. Su, *Angew. Chem., Int. Ed.*, 2021, **60**, 2089–2093.
42 H. Ding, W. Guo and B. Su, *Angew. Chem., Int. Ed.*, 2020, **59**, 449–456.
43 H. Ding, P. Zhou, W. Fu, L. Ding, W. Guo and B. Su, *Angew. Chem., Int. Ed.*, 2021, **60**, 11769–11773.
44 K. Ino, K. Komatsu, K. Hiramoto, Y. Utagawa, Y. Nashimoto and H. Shiku, *Electrochim. Acta*, 2022, **415**, 140240.
45 X. Qin, H.-J. Jin, X. Li, J. Li, J.-B. Pan, K. Wang, S. Liu, J.-J. Xu and X.-H. Xia, *Chem. – Eur. J.*, 2022, **28**, e202103964.
46 L. Ding, H. Ding, P. Zhou, L. Xi and B. Su, *Anal. Chem.*, 2022, **94**, 10885–10892.
47 B. Rothenhäusler and W. Knoll, *Nature*, 1988, **332**, 615–617.
48 Y. Fang, H. Wang, H. Yu, X. Liu, W. Wang, H.-Y. Chen and N. J. Tao, *Acc. Chem. Res.*, 2016, **49**, 2614–2624.
49 W. Wang, Y. Yang, S. Wang, V. J. Nagaraj, Q. Liu, J. Wu and N. Tao, *Nat. Chem.*, 2012, **4**, 846–853.
50 A. W. Peterson, M. Halter, A. Tona and A. L. Plant, *BMC Cell Biol.*, 2014, **15**, 35.
51 Y. Yang, H. Yu, X. Shan, W. Wang, X. Liu, S. Wang and N. Tao, *Small*, 2015, **11**, 2878–2884.
52 R. Robelek and J. Wegener, *Biosens. Bioelectron.*, 2010, **25**, 1221–1224.
53 W. Wang, K. Foley, X. Shan, S. Wang, S. Eaton, V. J. Nagaraj, P. Wiktor, U. Patel and N. Tao, *Nat. Chem.*, 2011, **3**, 249–255.
54 X.-W. Liu, Y. Yang, W. Wang, S. Wang, M. Gao, J. Wu and N. Tao, *Angew. Chem., Int. Ed.*, 2017, **56**, 8855–8859.
55 L. Berguiga, L. Streppa, E. Boyer-Provera, C. Martinez-Torres, L. Schaeffer, J. Elezgaray, A. Arneodo and F. Argoul, *Appl. Opt.*, 2016, **55**, 1216–1227.
56 J. Lu, Y. Yang, W. Wang, J. Li, N. Tao and S. Wang, *Anal. Chem.*, 2016, **88**, 11498–11503.

57 K. Toma, H. Kano and A. Offenhäusser, *ACS Nano*, 2014, **8**, 12612–12619.
58 K. F. Giebel, C. Bechinger, S. Herminghaus, M. Riedel, P. Leiderer, U. Weiland and M. Bastmeyer, *Biophys. J.*, 1999, **76**, 509–516.
59 K. Watanabe, K. Matsuura, F. Kawata, K. Nagata, J. Ning and H. Kano, *Biomed. Opt. Express*, 2012, **3**, 354–359.
60 E. Kreysing, H. Hassani, N. Hampe and A. Offenhäusser, *ACS Nano*, 2018, **12**, 8934–8942.
61 S. Dai, T. Yu, J. Zhang, H. Lu, J. Dou, M. Zhang, C. Dong, J. Di and J. Zhao, *Biosens. Bioelectron.*, 2021, **174**, 112826.
62 W. Wang, S. Wang, Q. Liu, J. Wu and N. Tao, *Langmuir*, 2012, **28**, 13373–13379.
63 E. Kreysing, S. Seyock, H. Hassani, E. Brauweiler-Reuters, E. Neumann and A. Offenhäusser, *Adv. Mater. Interfaces*, 2020, **7**, 1901991.
64 S.-H. Kim, W. Chegal, J. Doh, H. M. Cho and D. W. Moon, *Biophys. J.*, 2011, **100**, 1819–1828.
65 A. W. Peterson, M. Halter, A. Tona, A. L. Plant and J. T. Elliott, presented in part at the Conference on Plasmonics in Biology and Medicine XV, San Francisco, CA, Jan 29, 2017.
66 Y. Zeng, J. Zhou, X. Wang, Z. Cai and Y. Shao, *Biosens. Bioelectron.*, 2019, **145**, 111717.
67 P. Zhang, X. Zhou, R. Wang, J. Jiang, Z. Wan and S. Wang, *ACS Sens.*, 2021, **6**, 4244–4254.
68 P. Zhang, X. Zhou, J. Jiang, J. Kolay, R. Wang, G. Ma, Z. Wan and S. Wang, *Angew. Chem., Int. Ed.*, 2022, **61**, e202209469.
69 Y. Cho, E. Y. Park, E. Ko, J.-S. Park and J. H. Shin, *Int. J. Precis. Eng. Man.*, 2016, **17**, 1401–1412.
70 S. S. Hur, J. H. Jeong, M. J. Ban, J. H. Park, J. K. Yoon and Y. Hwang, *BMB Rep.*, 2020, **53**, 74–81.
71 A. K. Nguyen and K. A. Kilian, *ACS Chem. Biol.*, 2020, **15**, 1731–1746.
72 A. Simon and M.-C. Durrieu, *Micron*, 2006, **37**, 1–13.
73 J. Helenius, C.-P. Heisenberg, H. E. Gaub and D. J. Muller, *J. Cell Sci.*, 2008, **121**, 1785–1791.
74 K. Haase and A. E. Pelling, *J. R. Soc., Interface*, 2015, **12**, 20140970.
75 C. Arbore, L. Perego, M. Sergides and M. Capitanio, *Biophys. Rev.*, 2019, **11**, 765–782.
76 C. Guilluy, L. D. Osborne, L. Van Landeghem, L. Sharek, R. Superfine, R. Garcia-Mata and K. Burridge, *Nat. Cell Biol.*, 2014, **16**, 376–381.
77 Y. Tu and X. Wang, *Sensors*, 2020, **20**, 7128.
78 Q. Tian, P. Keshri and M. You, *Chem. Commun.*, 2022, **58**, 4700–4710.
79 T. G. Kapp, F. Rechenmacher, S. Neubauer, O. V. Maltsev, E. A. Cavalcanti-Adam, R. Zarka, U. Reuning, J. Notni, H.-J. Wester, C. Mas-Moruno, J. Spatz, B. Geiger and H. Kessler, *Sci. Rep.*, 2017, **7**, 39805.
80 L. S. Fischer, S. Rangarajan, T. Sadhanasatish and C. Grashoff, *Annu. Rev. Biophys.*, 2021, **50**, 595–616.
81 Y. Liu, K. Galior, V. P.-Y. Ma and K. Salaita, *Acc. Chem. Res.*, 2017, **50**, 2915–2924.
82 D. R. Stabley, C. Jurchenko, S. S. Marshall and K. S. Salaita, *Nat. Methods*, 2012, **9**, 64–67.
83 A. C. Chang, A. H. Mekhdjian, M. Morimatsu, A. K. Denisin, B. L. Pruitt and A. R. Dunn, *ACS Nano*, 2016, **10**, 10745–10752.
84 K. Galior, Y. Liu, K. Yehl, S. Vivek and K. Salaita, *Nano Lett.*, 2016, **16**, 341–348.
85 C. Jurchenko, Y. Chang, Y. Narui, Y. Zhang and K. S. Salaita, *Biophys. J.*, 2014, **106**, 1436–1446.
86 Y. Liu, K. Yehl, Y. Narui and K. Salaita, *J. Am. Chem. Soc.*, 2013, **135**, 5320–5323.
87 Y. Liu, R. Medda, Z. Liu, K. Galior, K. Yehl, J. P. Spatz, E. A. Cavalcanti-Adam and K. Salaita, *Nano Lett.*, 2014, **14**, 5539–5546.
88 C. Grashoff, B. D. Hoffman, M. D. Brenner, R. Zhou, M. Parsons, M. T. Yang, M. A. McLean, S. G. Sligar, C. S. Chen, T. Ha and M. A. Schwartz, *Nature*, 2010, **466**, 263–266.
89 M. Morimatsu, A. H. Mekhdjian, A. S. Adhikari and A. R. Dunn, *Nano Lett.*, 2013, **13**, 3985–3989.
90 S. J. Tan, A. C. Chang, S. M. Anderson, C. M. Miller, L. S. Prahl, D. J. Odde and A. R. Dunn, *Sci. Adv.*, 2020, **6**, eaax0317.
91 M. Rief, M. Gautel, F. Oesterhelt, J. M. Fernandez and H. E. Gaub, *Science*, 1997, **276**, 1109–1112.
92 M. M. F. A. Baig, W.-F. Lai, M. F. Akhtar, A. Saleem, S. A. Ahmed and X.-H. Xia, *Nano-Struct. Nano-Objects*, 2020, **23**, 100523.
93 C. Albrecht, K. Blank, M. Lalic-Mülthaler, S. Hirler, T. Mai, I. Gilbert, S. Schiffmann, T. Bayer, H. Clausen-Schaumann and H. E. Gaub, *Science*, 2003, **301**, 367–370.
94 K. Hatch, C. Danilowicz, V. Coljee and M. Prentiss, *Phys. Rev. E*, 2008, **78**, 011920.
95 M. Roein-Peikar, Q. Xu, X. Wang and T. Ha, *Phys. Rev. X*, 2016, **6**, 011001.
96 X. Wang and T. Ha, *Science*, 2013, **340**, 991–994.
97 X. Wang, Z. Rahil, I. T. S. Li, F. Chowdhury, D. E. Leckband, Y. R. Chemla and T. Ha, *Sci. Rep.*, 2016, **6**, 21584.
98 Y. Wang and X. Wang, *Sci. Rep.*, 2016, **6**, 36959.
99 K. A. Kim, S. Vellampatti, S. H. Hwang and B. C. Kim, *Adv. Funct. Mater.*, 2022, **32**, 2110637.
100 Y. Wang, D. N. LeVine, M. Gannon, Y. Zhao, A. Sarkar, B. Hoch and X. Wang, *Biosens. Bioelectron.*, 2018, **100**, 192–200.
101 Y. Zhao, Y. Wang, A. Sarkar and X. Wang, *iScience*, 2018, **9**, 502–512.
102 M. H. Jo, B. C. Kim, K. Sung, R. A. Panettieri, S. S. An, J. Liu and T. Ha, *ACS Nano*, 2021, **15**, 11585–11596.
103 S. A. Rashid, A. T. Blanchard, J. D. Combs, N. Fernandez, Y. Dong, H. C. Cho and K. Salaita, *ACS Nano*, 2022, **16**, 5335–5348.
104 Y. Zhao, K. Pal, Y. Tu and X. Wang, *J. Am. Chem. Soc.*, 2020, **142**, 6930–6934.
105 K. Pal, Y. Tu and X. Wang, *ACS Nano*, 2022, **16**, 2481–2493.
106 M. H. Jo, W. T. Cottle and T. Ha, *ACS Biomater. Sci. Eng.*, 2019, **5**, 3856–3863.
107 Y. Zhang, C. Ge, C. Zhu and K. Salaita, *Nat. Commun.*, 2014, **5**, 5167.
108 B. L. Blakely, C. E. Dumelin, B. Trappmann, L. M. McGregor, C. K. Choi, P. C. Anthony, V. K. Duesterberg, B. M. Baker, S. M. Block, D. R. Liu and C. S. Chen, *Nat. Methods*, 2014, **11**, 1229–1232.
109 Y. Zhang, Y. Qiu, A. T. Blanchard, Y. Chang, J. M. Brockman, V. P.-Y. Ma, W. A. Lam and K. Salaita, *Proc. Natl. Acad. Sci. U. S. A.*, 2018, **115**, 325–330.
110 Y. Liu, L. Blanchfield, V. P.-Y. Ma, R. Andargachew, K. Galior, Z. Liu, B. Evavold and K. Salaita, *Proc. Natl. Acad. Sci. U. S. A.*, 2016, **113**, 5610–5615.
111 R. Ma, A. V. Kellner, V. P.-Y. Ma, H. Su, B. R. Deal, J. M. Brockman and K. Salaita, *Proc. Natl. Acad. Sci. U. S. A.*, 2019, **116**, 16949–16954.
112 J. M. Brockman, A. T. Blanchard, V. Pui-Yan, W. D. Derricotte, Y. Zhang, M. E. Fay, W. A. Lam, F. A. Evangelista, A. L. Mattheyses and K. Salaita, *Nat. Methods*, 2018, **15**, 115–118.
113 J. M. Brockman, H. Su, A. T. Blanchard, Y. Duan, T. Meyer, M. E. Quach, R. Glazier, A. Bazrafshan, R. L. Bender, A. V. Kellner, H. Ogasawara, R. Ma, F. Schueder, B. G. Petrich, R. Jungmann, R. Li, A. L. Mattheyses, Y. Ke and K. Salaita, *Nat. Methods*, 2020, **17**, 1018–1024.
114 T. Schlichthaerle, C. Lindner and R. Jungmann, *Nat. Commun.*, 2021, **12**, 2510.
115 H. Li, C. Zhang, Y. Hu, P. Liu, F. Sun, W. Chen, X. Zhang, J. Ma, W. Wang, L. Wang, P. Wu and Z. Liu, *Nat. Cell Biol.*, 2021, **23**, 642–651.
116 S. J. Sahl, S. W. Hell and S. Jakobs, *Nat. Rev. Mol. Cell Biol.*, 2017, **18**, 685–701.
117 D. F. Kelly, D. W. Taylor, C. Bakolitsa, A. A. Bobkov, L. Bankston, R. C. Liddington and K. A. Taylor, *J. Mol. Biol.*, 2006, **357**, 562–573.
118 X. Barros-Álvarez, R. M. Nwokonko, A. Vizurraga, D. Matzov, F. He, M. M. Papasergi-Scott, M. J. Robertson, O. Panova, E. H. Yardeni, A. B. Seven, F. E. Kwarcinski, H. Su, M. C. Peroto, J. G. Meyerowitz, M. Shalev-Benami, G. G. Tall and G. Skiniotis, *Nature*, 2022, **604**, 757–762.
119 X. P. Xu, S. Pokutta, M. Torres, M. F. Swift, D. Hanein, N. Volkmann and W. I. Weis, *eLife*, 2020, **9**, e60878.